THE JOURNAL OF PHYSICAL CHEMISTRY A

Article

pubs.acs.org/JPCA

Role of Proton Hopping in Surface Charge Transport on Tin Dioxide As Revealed by the Thermal Dependence of Conductance

Robert B. Wexler[†] and Karl Sohlberg*

Department of Chemistry, Drexel University, Philadelphia, Pennsylvania 19104, United States

Supporting Information

ABSTRACT: The presence of water on an oxide surface can dramatically alter its electrical properties with important consequences for electrical measurements by scanning probe microscopy, and for the use of semiconducting oxides in sensing applications. Here, the thermal dependence of the conductance of tin dioxide is interpreted by combining semiconductor equilibrium carrier statistics with a proton hopping mechanism. First, the functional form of this charge transport model is fit to experimental conductance data for tin dioxide. Next, the important energy parameters in the model are computed with density functional theory. Comparing the values of the energy parameters obtained by fitting, to the values for the same parameters obtained from electronic structure calculations, yields new insight into the surface charge transport in tin dioxide. In particular, it is found that mobile protons, freed from the dissociative adsorption of water on the [110] surface, are an essential component of the observed thermal dependence of conductance in tin dioxide.

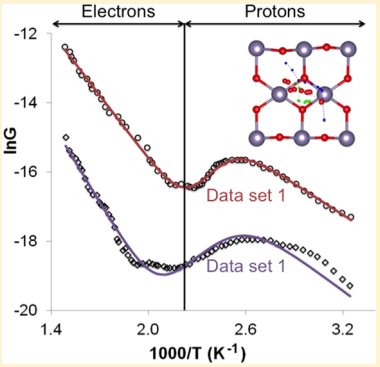

1. INTRODUCTION

Tin dioxide is a versatile wide-bandgap semiconductor that finds use in the fields of optoelectronics, heterogeneous catalysis, and gas sensing, for which the following applications serve as representative examples. (i) Thin film solar cells are often coated with indium tin oxide, a solid solution of indium(III) and tin(IV) oxide, which is both optically transparent and conductive.[1] (ii) The dual valency of tin allows for the catalysis of small molecule oxidation reactions through the Mars−van Krevelen mechanism.[2] (iii) Gas molecules, such as carbon monoxide, readily adsorb to the surface of tin dioxide, inducing detectable changes in the conductance.[3]

All of the above applications depend on the electronic properties of SnO_2, the latter two on surface conductance and its response to the presence of a surface adsorbate. An especially relevant surface adsorbate is water, not only because water is ubiquitous but also because it can serve as a source of protons, which are potential charge carriers. The presence of adsorbed water is therefore of potentially considerable significance because protonic conductivity contributes to charge transport in many different systems. For example, Stoica et al. reported that mobile hydrogen species in Pt/Al_2O_3 films must be protons due to accompanying conductivity effects.[4] A similar phenomenon was observed by Caldararu et al. for γ-alumina.[5] Caldararu's findings were corroborated by Cai et al., who tested a dual-charge-carrier model for the conductance of γ-alumina and validated the model with electronic structure calculations.[6,7] It was found that hydrogen-bonded water molecules serve as a scaffold for mobile protons at temperatures below the threshold for thermal desorption of water. Kavasoglu and Bayhan have observed similar ion hopping and diffusion in $ZnCr_2O_4$−K_2CrO_4, a semiconducting ceramic composite.[8]

In this investigation, the thermal dependence of surface conductance of SnO_2 is modeled with an expression that includes contributions from both electronic carriers and proton hopping. Such mixed electron and proton charge transport is not unprecedented. Examples relevant to the present study include its observation in a perovskite oxide[9] and a nanocomposite.[10] The model developed here accounts for an anomalous feature in the experimental Arrhenius plot of electrical conductance for SnO_2 and consequently gives insight into the role of adsorbed water in the surface conductance of tin dioxide. The results imply that variations in humidity could significantly alter the conductance of tin dioxide-based devices that operate between 300 and 450 K.

2. BACKGROUND

2.1. Hypothesis. Tin dioxide is an oxygen deficient, n-type semiconductor. The defect free material has a direct band gap of 3.6 eV at the Γ-point.[11] The band gap decreases and becomes indirect in the presence of oxygen vacancies (vide infra). Tin dioxide adopts the rutile crystal structure and prefers cleavage along the [110] plane.[2] Figure 1 shows the thermal dependence of conductance for tin dioxide powder between 300 and 700 K. (Data courtesy of the late M. Caldararu.[12])

The temperature dependence of conductance for semiconducting, gas sensing materials is often modeled using the

Special Issue: David R. Yarkony Festschrift

Received: July 30, 2014
Revised: October 2, 2014
Published: October 2, 2014

   dx.doi.org/10.1021/jp5076719 | J. Phys. Chem. A 2014, 118, 12031−12040

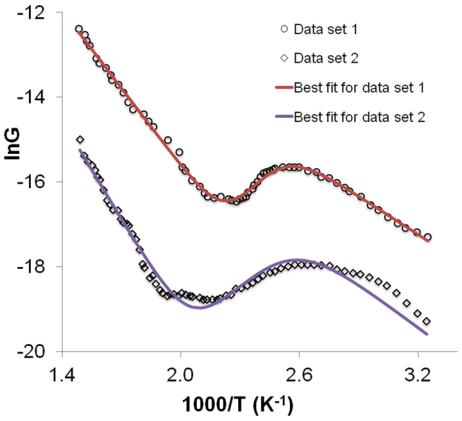

Figure 1. Thermal dependence of conductance for tin dioxide showing two independent sets of experimental data and our best-fit model.

Arrhenius equation,[13−15] which predicts a linear relationship between ln G vs T^{-1}. Tin dioxide, however, shows an anomalous "bump" in the Arrhenius plot ca. 400 K.

Water, being ubiquitous, could conceivably play a role in this anomaly by serving as a source of protons, which may in turn transport charge. Such a role for water would not be unprecedented. A similar anomaly in the thermal dependence of surface conductance of γ-alumina can be attributed to proton hopping among adsorbed water molecules.[6] Further evidence of the role of water in the thermal dependence of surface conductance of SnO_2 comes from Scurtu et al.,[16] who, upon heating alumina-supported SnO_2 under a flow of dry argon, reported the evolution of water in the effluent between ca. 373−573 K. Additional evidence of the role of water was reported by Caldararu et al.,[17] who found the low-temperature conductance of SnO_2 powder is much lower during the second and later cycles when measured for successive heat−cool cycles under a flow of dry inert gas (i.e., after one drying cycle, there was a dramatic drop in conductance, especially at the low end of the 373−673 K temperature range of the thermal cycle). Shen et al. also observed intermediate-temperature proton conduction and water evolution, via electromotive force and temperature-programmed desorption measurements, respectively.[18]

On the strength of the above evidence, we hypothesize that water molecules adsorbed to the surface of tin dioxide contribute to the conductance through proton hopping. This would account not only for the initial increase in conductance from 300 to 400 K (because increasing the thermal energy will contribute to increased proton mobility) but also for the decrease in conductance from 400 to 450 K, if it is found that the binding energy of water to the SnO_2 surface is such that water thermally desorbs above ca. 400 K. Increases in conductance above 450 K can be attributed to conventional (semiconductor) transport processes.

2.2. Model. To test the above hypothesis, a dual-charge-carrier model was developed that includes the contributions of both electrons and mobile surface protons to the conductance. The relationship between conductance (G) and conductivity (σ) is

$$G = \frac{A}{l}\sigma \tag{1}$$

Collecting the geometric parameters, area (A) and length (l) (as well as instrument-dependent extrinsic factors) into a fitting parameter (B), and given that conductivity can be expressed in terms of the charges (e), concentrations (n), and mobilities (μ) of the individual carriers ($\sigma = \mu en$), when these two types of charge carriers are present, conductance may be expressed as

$$G = B(en_e\mu_e + en_p\mu_p) \tag{2}$$

where the "e" and "p" subscripts denote the electronic and protonic charge carriers.

2.2.1. Electron Term. The functional dependence of electron concentration (n_e) on temperature (T) for an n-type semiconductor is textbook semiconductor physics[19]

$$n_e = \frac{\left(\frac{N_C}{g_D}\right)\exp\left(-\frac{E_g}{k_BT}\right)}{2}\left(\sqrt{1 + \frac{4N_d}{\left(\frac{N_C}{g_D}\right)\exp\left(-\frac{E_g}{k_BT}\right)}} - 1\right) \tag{3}$$

Here N_C is the effective density of states at the conduction band minimum and its thermal dependence is $N_C = 2(2\pi m_n^* k_B T/h^2)^{3/2}$. k_B is the Boltzmann constant. g_D, the donor-site spin degeneracy factor, is 2 for Fermionic charge carriers.[19] E_g is the energy gap between a donor state and the conduction band minimum. N_d is the total donor concentration. In tin dioxide, oxygen vacancies are the primary donors of electronic charge carriers.[2] Equation 3 only describes $n_e(T)$ in the "freeze out" temperature region. In this region, donor impurities are ionized, freeing electrons for conduction.[19] The intrinsic temperature region is not considered because tin dioxide has a wide band gap. It would require temperatures higher than 700 K to excite a non-negligible number of electrons across the 3.6 eV band gap. Intrinsic semiconductor behavior therefore does not contribute to $G(T)$ in SnO_2 in the temperature regime of interest here.

We model the thermal dependence of N_d with the Boltzmann distribution

$$N_d = N_p \exp\left(-\frac{E_v}{k_BT}\right) \tag{4}$$

where N_p is the concentration of potential oxygen vacancy sites and E_v is the oxygen vacancy formation energy.

Kim and Park found that variation in the thermal dependence of the electronic conductivity for tin oxide films between 300 and 700 K could be attributed primarily to electron concentration rather than mobility, $\sigma_e(T) = en_e(T)\text{-}\mu_e$.[20] We therefore assume that the electron mobility is effectively temperature independent between 300 and 700 K.

2.2.2. Proton Term. For the proton term, the Langmuir isotherm[21] was used to express the concentration of surface charge carriers (n_p). Under this assumption, the T-dependence of n_p is given by

$$n_p(T) = N_w\Theta_w(T) \tag{5}$$

Here, N_w is the total concentration of potential water adsorption sites and Θ_w is the Langmuir equation for the fractional coverage of the surface by water. Θ_w can be written as

$$\Theta_w = \frac{P_w \exp\left(\frac{\Delta S}{k_B}\right)\exp\left(-\frac{E_w}{k_BT}\right)}{1 + P_w \exp\left(\frac{\Delta S}{k_B}\right)\exp\left(-\frac{E_w}{k_BT}\right)} \tag{6}$$

dx.doi.org/10.1021/jp5076719 | J. Phys. Chem. A 2014, 118, 12031−12040

where P_w is the partial pressure of water vapor, ΔS is the entropy of water adsorption, and E_w is the energy change during adsorption.[6]

Within the bulk of an oxide, protons hop between sites where they are associated with an adjacent oxygen.[22] Detailed theoretical analyses of proton hopping have been reported for perovskite oxides by Matsushita and co-workers,[23,24] and at oxide interfaces by Tocci and Michaelides.[25] To determine the mobility (μ_p) of protons moving by such a mechanism, Boltzmann probabilities may be used to determine the rate at which protons overcome the hopping barrier between adjacent sites.[22] The same concept is applied here. When adsorbed to a surface, a proton vibrates at a frequency ν_j about its adsorption site. To transport charge, the proton must jump a distance, d_j, across a potential energy barrier (E_j) separating two adjacent surface sites. The probability (P_j) that a proton overcomes E_j is

$$P_j = \exp\left(-\frac{E_j}{k_B T}\right) \tag{7}$$

When a proton hops in the same direction as the applied electric field (E), E_j is lowered by ($Eqd_j/2$), where q is the proton charge. When a proton hops in the reverse direction, E_j is increased by ($Eqd_j/2$). The drift velocity of a proton (v_p) is

$$v_p = \nu_j d_j \left[\exp\left(-\frac{E_j - \frac{Eqd_j}{2}}{k_B T}\right) + \exp\left(-\frac{E_j + \frac{Eqd_j}{2}}{k_B T}\right)\right] \tag{8}$$

Noting that μ is a proportionality constant between the drift velocity (v) and E, eq 8 can be rewritten as

$$\mu_p = \frac{\nu_j d_j}{E}\left[\exp\left(-\frac{E_j - \frac{Eqd_j}{2}}{k_B T}\right) + \exp\left(-\frac{E_j + \frac{Eqd_j}{2}}{k_B T}\right)\right] \tag{9}$$

2.2.3. Full Model. Substituting eqs 3, 5, and 9 into eq 2 produces a complete expression for the thermal dependence of conductance for tin dioxide, assuming that there are only two types of charge carriers, electrons and protons,

$$G = Be\left[\frac{\left(\frac{2\pi m_n^* k_B T}{h^2}\right)^{3/2}\exp\left(-\frac{E_g}{k_B T}\right)}{2}\right.$$
$$\times\left(\sqrt{1 + \frac{4N_p \exp\left(-\frac{E_v}{k_B T}\right)}{\left(\frac{2\pi m_n^* k_B T}{h^2}\right)^{3/2}\exp\left(-\frac{E_g}{k_B T}\right)}} - 1\right)\mu_e$$
$$+ N_w \frac{P_w \exp\left(\frac{\Delta S}{k_B}\right)\exp\left(-\frac{E_w}{k_B T}\right)}{1 + P_w \exp\left(\frac{\Delta S}{k_B}\right)\exp\left(-\frac{E_w}{k_B T}\right)}\frac{\nu_j d_j}{E}$$
$$\left.\times\left[\exp\left(-\frac{E_j - \frac{Eqd_j}{2}}{k_B T}\right) + \exp\left(-\frac{E_j + \frac{Eqd_j}{2}}{k_B T}\right)\right]\right] \tag{10}$$

Grouping all of the temperature-independent terms into fitting parameters and simplifying the quotient of exponentials under the square root sign, eq 10 becomes

$$G = A\left[BT^{3/2}\exp\left(-\frac{E_g}{k_B T}\right)\right.$$
$$\times\left(\sqrt{1 + CT^{-3/2}\exp\left(\frac{E_g - E_v}{k_B T}\right)} - 1\right)$$
$$+ D\frac{\exp\left(-\frac{E_w}{k_B T}\right)}{1 + P\exp\left(-\frac{E_w}{k_B T}\right)}\times\left[\exp\left(-\frac{E_j - F}{k_B T}\right)\right.$$
$$\left.\left.+ \exp\left(-\frac{E_j + F}{k_B T}\right)\right]\right] \tag{11}$$

This functional form of the model (eq 11) was fit to the experimental data by optimizing the overall scaling parameters (A, B, C, D, and P) and the energy parameters (E_g, E_v, E_w, E_j, F). Agreement of the fitted curve with the experimental data is excellent (Figure 1). The energy parameters in the model were also computed using electronic structure calculations and compared to the equivalent values obtained by fitting the model.

Equation 11 contains both energy and overall scaling parameters. The energy parameters are intrinsic to the material whereas the overall scaling parameters depend on the experimental conditions, which can vary from lab to lab or even experiment to experiment due to such factors as contact resistance, internal resistance of the measuring apparatus, vapor pressure, etc. In this work, we focus on validating the energy parameters because they are more invariant with environmental changes and are directly predictable from density functional theory total energy and band structure calculations. It is difficult to ascribe physical meaning to the scaling parameters A, B, C, D, and P, although some can be identified as being *influenced* by one or more particular physical quantities. (P, for example, is the product a units conversion factor, the water partial pressure, and $\exp(\Delta S/k_B)$ where ΔS is the entropy change upon water adsorption.) It should be noted that the model is much more sensitive to the energy parameters, as shown in Figure S1 in the Supporting Information.

The present model is similar to one derived by Cai et al.[6] to describe the thermal dependence of conductance for γ-alumina. The functional form of their model is

$$G = A\sum_{i=1}^{N}\left[\nu_i d_i\left[\exp\left(\frac{\Delta\xi_i}{k_B}\right)\exp\left(-\frac{\Delta\epsilon_i - Eq_i d_i/2}{k_B T}\right)\right.\right.$$
$$\left.- \exp\left(\frac{\Delta\xi_i}{k_B}\right)\exp\left(-\frac{\Delta\epsilon_i + Eq_i d_i/2}{k_B T}\right)\right]$$
$$\left.\times N_i\frac{P_i \exp\left(\frac{\Delta S_i}{k_B T}\right)\exp\left(-\frac{\Delta E_i}{k_B T}\right)}{1 + P_i \exp\left(\frac{\Delta S_i}{k_B T}\right)\exp\left(-\frac{\Delta E_i}{k_B T}\right)}\right] \tag{12}$$

dx.doi.org/10.1021/jp5076719 | J. Phys. Chem. A 2014, 118, 12031−12040

Table 1. Results of Our Calculations for Several Different Parameters Associated with the SnO_2 System along with Values from the Literature and, Where Applicable, Values Determined by Fitting Eq 11 to Experimental $G(T)$ Data[a]

parameter	lit. value (units)	B3LYP	GGA	LDA	fit
a	expt[2] 4.7374 (Å)	4.70	4.92	4.69	NA
c	expt[2] 3.1864 (Å)	3.20	3.30	3.16	NA
cell volume (a^2c)	expt[2] 71.51 (Å^3)	70.59 (−2%)	79.97 (+12%)	69.31 (−3%)	NA
band gap (E_g)	expt[11] 3.6 (eV)	3.7	0.42	1.3	3.6 ($\delta \approx 0$)
surface gap ($E_{g,s}$)	theo[37] 2.41 (eV)	**2.53**	0.21	0.93	NA
surface energy (E_s)	theo[38] 1.21 (J/m^2)	1.98	2.14	**1.80**	NA
	theo[39] 1.401				
	theo[40] 1.56				
bulk oxygen vacancy formation energy ($E_{v,b}$)	theo[41] 3.49 (eV)	7.62	3.85	5.83	0.60 (δ = 0.14)
surface oxygen vacancy formation energy ($E_{v,s}$)	theo[42] 2.27 (eV)	5.72	**0.60**	4.49	
gap in the presence of a surface O vacancy	theo[37] 0.9 (eV)	1.92	0.07	0.67	0.38 (δ = 0.28)
water adsorption energy (E_w)	theo[43] −1.0 (eV)	−1.93	**−1.36**	−2.46	−0.86 (δ = 0.26)
	theo[44] −1.02 (associative)				
	−1.4 (dissociative)				

[a]The fitted value is the average of the two sets of experimental data. (δ denotes the range of values obtained from the two different fits, i.e., the difference between the two values found). Where no experimental value is available, our recommended theoretical value is reported in underlined boldface. (See text for rationale.) The fit does not distinguish between bulk and surface oxygen vacancies; thus, only one value is given.

where i is an index for the ith charge carrier, and $\Delta\xi$ is the entropic contribution to the hopping barrier. A, $\Delta\epsilon$, ΔS, and ΔE are analogous to A, E_j, ΔS, and E_w in eq 10. Because γ-alumina is a wide band gap insulator, electronic terms (i.e., the first two rows of eq 11) are not relevant. SnO_2, however, is a semiconductor so both electronic and protonic carriers must be modeled.

2.3. Electronic Structure Calculations. Density functional theory (DFT) based electronic structure calculations were employed in this investigation to estimate the energy parameters in the $G(T)$ model.

Calculations using the LDA (CA,[26] -PZ[27]) and GGA (PBE[28]) exchange−correlation functionals were performed using the CASTEP code implemented in Materials Studio by Accelrys.[29] Calculations performed with CASTEP used a plane-wave basis set to describe the valence electron density and pseudopotentials to describe the interactions of the valence electrons with the atomic cores. The basis set was defined using a 380 eV energy cutoff for LDA calculations and 340 eV energy cutoff for GGA calculations. The convergence criteria for both the LDA and GGA calculations were as follows: 2×10^{-5} eV/atom (energy), 0.05 eV/Å (max force), 0.1 GPa (max stress), and 0.002 Å (max displacement). The final four criteria refer only to relaxations of the cell parameters and ionic positions.

Density functional theory calculations using the B3LYP[30,31] hybrid exchange−correlation functional were performed using the CRYSTAL09 package.[32] The basis set (composed of atom-centered functions) for calculations with CRYSTAL09 was as follows: for tin, three Gaussian functions were used for the valence orbitals (two 5sp and one 5p)[33] whereas the interactions of the valence electrons with the Sn cores were described with the DURAND pseudopotential.[34] For oxygen, the basis set was the same as that used by Causà et al. for magnesium oxide.[35] For the oxygen vacancy calculations, ghost atoms with oxygen basis sets were centered at the vacancy sites. An extra large FFT grid, consisting of 75 radial and 974 angular points, was used for tin. A total of 200 points were allowed in a batch for numerical integration. 4 × 4 × 4, 8 × 8 × 8, and 12 × 12 × 12 Pack−Monkhorst−Gilat meshes were all tested on the bulk. The total energy difference between calculations employing the 8 × 8 × 8 and 12 × 12 × 12 meshes was 1.36×10^{-6} hartree per formula unit; this is 2 orders of magnitude smaller than the difference between the results of calculations with the 4 × 4 × 4 and 8 × 8 × 8 meshes. Therefore, calculations with the 8 × 8 × 8 mesh were judged to be suitably converged and the 8 × 8 × 8 mesh was used throughout. The energies of the occupied orbitals were reduced by 0.6 hartree and locked in an insulating state to abet convergence. Convergence was also accelerated using 30% Fock matrix mixing.

The convergence of the k-point grids (Table S1, Supporting Information) was tested in the bulk. The valence and conduction bands are almost flat (Figure S9, Supporting Information) so that the surface with a bridging oxygen vacancy should act as a direct band gap semiconductor. This justifies the use of 1 × 1 × 1 k-point grids for the GGA surface calculations.

Semiempirical PM6 calculations were performed in MOPAC.[36]

3. VALIDATION

The results of our calculations for several different parameters associated with the SnO_2 system are reported in Table 1 where they are compared with values from the literature and where applicable, with the values determined by fitting eq 11 to experimental $G(T)$ data.[12] Each is considered below.

3.1. Bulk Structure. The atomic positions and lattice parameters of bulk SnO_2 were obtained by full optimization of the primitive cell for tin dioxide shown in Figure 2. The bulk band gap and optimized lattice parameters for tin dioxide are given in Table 1.

The DFT-B3LYP, -GGA, and -LDA and calculations all give accurate estimates of the lattice parameters. Although -B3LYP and -LDA slightly outperform -GGA, the difference is not sufficient to justify a definitive choice of the best method.

3.2. Bulk and Surface Band Gap. Bulk band diagrams and density of states plots for tin dioxide can be found in the Supporting Information. The qualitative features in the band structure for bulk tin dioxide as captured in the band diagram are consistently predicted by the various DFT calculations (and a reference semiempirical calculation as well). One notable feature is the direct band gap at the center of the Brillouin zone, i.e., the Γ-point, for both the bulk and surface. The only appreciable differences among band diagrams are in the

dx.doi.org/10.1021/jp5076719 | J. Phys. Chem. A 2014, 118, 12031−12040

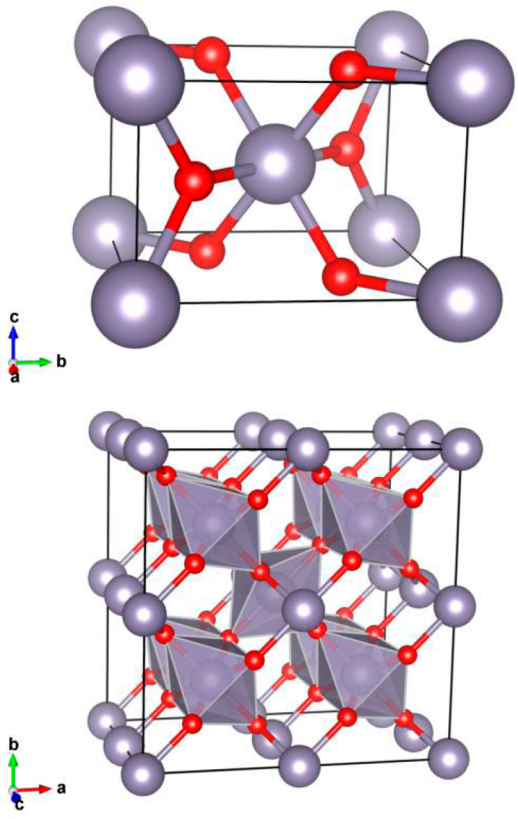

Figure 2. Ball and stick models of the *P*42/*mnm* (136), i.e., tetragonal, unit cell (left) and the LDA-optimized bulk tin dioxide (right). Tin atoms are purple and oxygen atoms are red. The polyhedra show that six oxygen atoms surround each tin atom in a distorted octahedral arrangement. The direction of the lattice vectors *a*, *b*, and *c* are shown by the axis labels. For rutile, |*a*| = |*b*|.

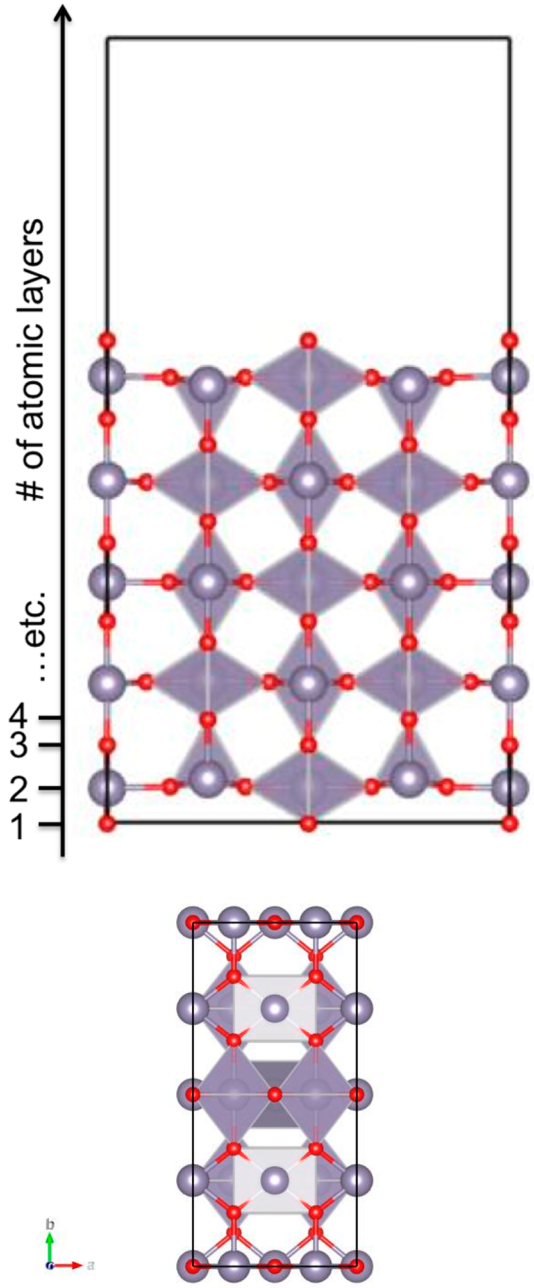

Figure 3. LDA-optimized ionic positions for a 15-layer slab with the [110] surface exposed, at the top and bottom, to 10 Å of vacuum space (left). Half of the surface tin atoms are under-coordinated, thus providing water adsorption sites. Bird's eye view of the [110] surface (right). The surface area is enclosed by the black box.

magnitude of the band gap. Among our calculations, the -B3LYP value is in by far the closest agreement with experiment. This is unsurprising because the B3LYP hybrid functional[30,31] has shown success in reliably predicting band gaps in related oxides and oxide surfaces.[45] We conclude that for the band gap, and surface gap calculations, DFT-B3LPY is the most reliable of the methods employed here.

3.3. Surface Energy. Using the optimized bulk lattice parameters, supercells were generated by translating the primitive cell in the a-, b-, and c-directions. The [110] surface was then cleaved from the supercells, producing the structures depicted in Figure 3.

The surface energy a predicted with a model surface slab containing n_f formula units was calculated using the following formula,

$$E_s = \frac{(E_{t,s} - n_f E_{t,b})}{2A_s} \quad (13)$$

where E_s is the surface energy, $E_{t,s}$ is the total energy of the surface slab, $E_{t,b}$ is the total energy of the primitive cell, and A_s is the area of the surface. The surface energy tends to be unreliable for surface slabs with too few layers. Therefore, E_s was plotted against the number of atomic layers (n_l) that were used in the surface model employed in the calculation to determine the number of layers needed to achieve convergence of E_s. The results are plotted in Figure 4.

The surface energy is fully converged at 9 layers for the DFT-B3LYP calculations. Calculations with the semiempirical PM6 Hamiltonian allowed for calculation up to 24 layers, which confirmed that convergence was reached by 9 layers. We therefore assume that the our DFT-LDA (15-layer surface slab) and -GGA (18-layer surface slab) surface energies reported in Table 1 are also converged with respect to increasing slab thickness. Figure 4 suggests that the literature value of surface energy from ref 38 may be too small because a 5-layer slab was used in that calculation and 5 layers produce a value less than the converged value.

dx.doi.org/10.1021/jp5076719 | J. Phys. Chem. A 2014, 118, 12031−12040

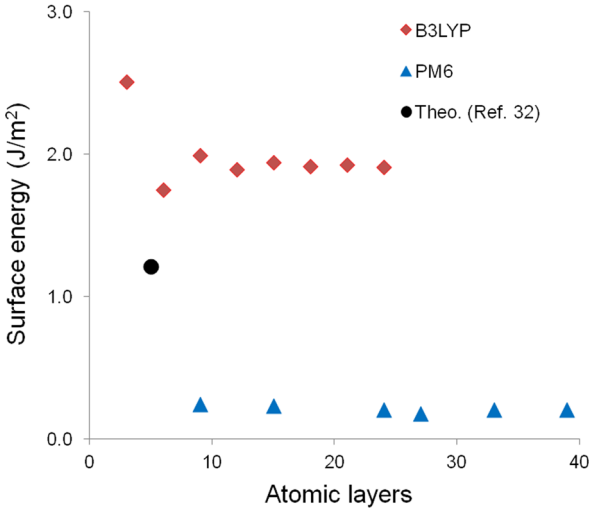

Figure 4. Convergence of surface energies calculated using the PM6 and DFT-B3LYP methodologies.

The DFT-B3LYP, -GGA, and -LDA surface energies are quite consistent, varying by just ±8%. This is consistent with earlier reports that found no clear preference for GGA or LDA in surface energy calculations.[46] More recent work, however, has shown a slight preference for LDA.[47] In recognition of this slight advantage of LDA, and the fact that our LDA result is in the best agreement with earlier (albeit possibly not fully converged) reports, we recommend the LDA value.

3.4. Vacancies. Oxygen vacancies were created in the bulk and at the [110] surface as shown in Figure 5.

The in-plane oxygen vacancy was unstable, causing a physically implausible distortion of the lattice during geometry optimization. Consequently, only bulk and bridging oxygen vacancies were considered as potential sources of electronic charge carriers in the "freeze out" temperature region. The oxygen vacancy formation energy was calculated as follows

$$E_{\mathrm{v}} = \left(E_{\mathrm{t,v}} + \frac{1}{2}E_{\mathrm{t,O_2}}\right) - E_{\mathrm{t,i}} \qquad (14)$$

where $E_{\mathrm{t,v}}$ is the total energy of a bulk supercell or [110] surface slab with an oxygen vacancy, $E_{\mathrm{t,O_2}}$ is the total energy of an oxygen molecule, and $E_{\mathrm{t,i}}$ is the total energy of a defect-free bulk supercell or [110] surface slab.

The DFT calculations all predict that a surface oxygen vacancy is energetically preferred over a bulk oxygen vacancy. Here one can make a strong case that the GGA calculation should be the most reliable, because one of the strengths of GGA is reliable treatment of bond breaking and bond forming processes,[48] which govern the formation of vacancies. Furthermore, the GGA $E_{\mathrm{v,s}}$ value is in excellent agreement with the fitting value, which is not experimentally distinguishable as surface or bulk. Our $E_{\mathrm{v,s}}$ value is also in agreement with literature GGA calculations by Tanaka et al.,[41] which also find that the most energetically stable vacancy is positively charged (+2). The GGA value should therefore probably be taken as an upper bound on the actual oxygen vacancy formation energy.

The penultimate row of Table 1 reports the band gap in the presence of a surface vacancy. Here there is no clear choice of theoretical method. The reliability of -B3LPY for computing band gaps[45] could be used as an argument to support that choice, but the importance of bond breaking processes in the formation of a vacancy could support the selection of -GGA as the best method.[48] It is even possible to argue for -LDA on the basis of the finding that -LDA is slightly preferred for surface energy calculations.[47] A conservative conclusion is that the band gap in the presence of a surface vacancy falls in the range covered by the three theoretical calculations [0.07−1.92 eV]. Selected band structures and density of states for defective tin dioxide can be found in the Supporting Information.

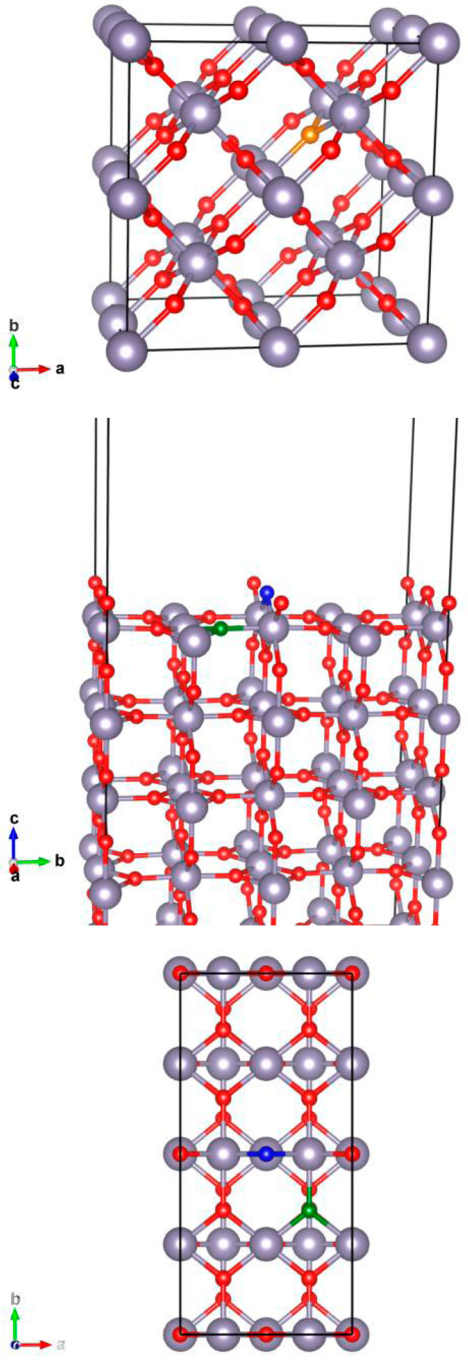

Figure 5. Bridging (blue), in-plane (green), and bulk oxygen vacancy sites (orange) on LDA-relaxed structures. The bridging and in-plane oxygen sites are on the [110] surface.

3.5. Water Adsorption. The dissociative adsorption of water is known to be thermodynamically favored on the [110] surface of tin dioxide.[49] The present DFT calculations all

dx.doi.org/10.1021/jp5076719 | J. Phys. Chem. A 2014, 118, 12031−12040

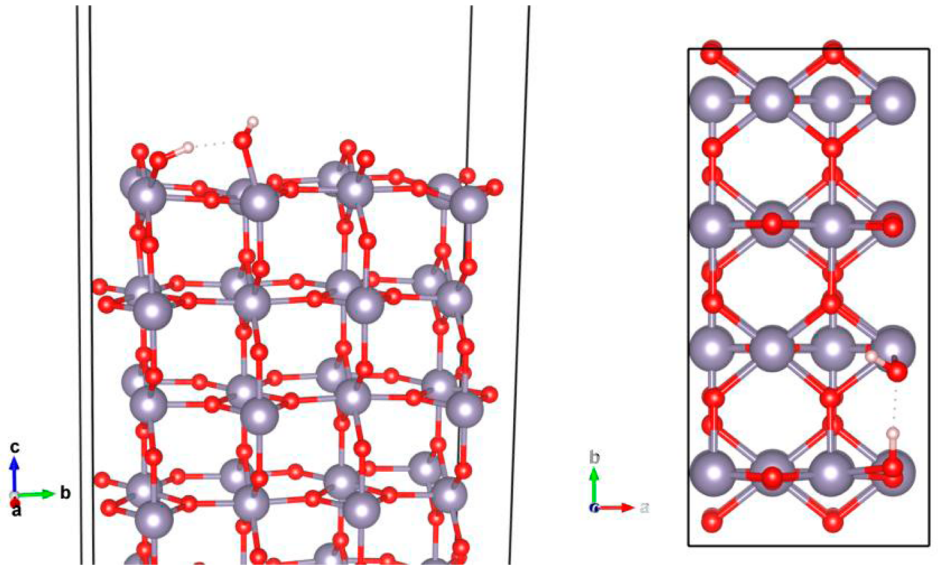

Figure 6. GGA structural optimization predicts the dissociative adsorption of water at the [110] surface of tin dioxide. The dotted line denotes an expected hydrogen bond between surface−OH species.

correctly predict the dissociative adsorption of water. The dissociated structure is shown in Figure 6.

The importance of bond-breaking and bond-forming processes in the dissociative adsorption of water argues strongly for favoring the GGA value.[48] Given that the GGA value is also in the best agreement with literature reports, it is recommended here. The B3LYP band diagram for the dissociative adsorption of water at the [110] surface of tin dioxide can be found in the Supporting Information. Note the striking similarity to the band diagram for the nondefective surface (also in the Supporting Information).

A series of constrained, PM6 optimization calculations, motivated by quadratic synchronous transit (QST),[50] was used to determine the minimum energy path of a proton across the surface. A semiempirical method was elected for this calculation to allow for the determination of the proton-hopping barrier within our computational resources. The lowest energy path is shown in Figure 7.

Starting from a PM6-optimized, 24-atomic-layer, (110) surface slab, the proton was moved in 0.3 Å increments along the $+z$ direction. Near the end of the path, the step size was changed to 0.1 Å. At each step a constrained optimization was carried out whereby the z coordinate of the proton was fixed but the proton was free to move throughout the xy plane. The geometry of the surface hydroxyl groups was conserved from start to finish. The computed energy barrier along this hopping path is 0.88 eV, which is of the same magnitude as the fitting value (0.64 eV). It is likely that the computed value is too high because computational demands preclude exhaustive searching of configuration space to identify the absolute minimum energy hopping path. In addition, reaction energy barriers tend to overestimated by HF-based electronic structure methods.[51,52] In particular, semiempirical methods overestimate barriers in proton transfer reactions.[53]

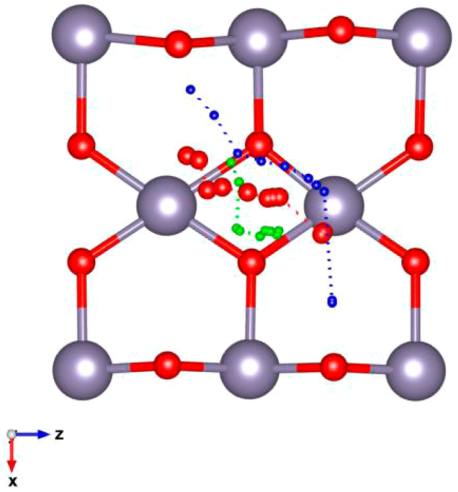

Figure 7. PM6 lowest energy, hopping path for a proton on the surface of tin dioxide using the QST method. Blue spheres are the hopping proton; green and smaller red spheres are hydrogen and oxygen respectively of the surface hydroxyl group bound to uncoordinated, in-plane, surface tin atoms. Each dot from left to right represents a step in the $+z$ direction.

4. RESULTS AND DISCUSSION

As shown by Table 1, the results of the fitting are in generally good agreement with those of the recommended electronic structure calculations: The recommended surface oxygen vacancy formation energy (0.71 eV) is close to the fitting value (0.6 eV, δ = 0.14). (Herein we use δ to denote the magnitude of the range of values obtained from the two different fits. For example, in the case of the oxygen vacancy formation energy we obtained values of 0.64 and 0.78 eV so we report the average 0.71 and the range δ = 0.14.) The recommended adsorption energy for water (−1.36 eV) is in reasonable agreement with the fitting value (−0.86 eV, δ = 0.26). Note that the magnitude of the adsorption energy decreases with increasing surface coverage of water,[43,49] so it is unsurprising that the fitting value, which surely corresponds to a hydrated surface, is lower in magnitude than the theoretical value, which corresponds to isolated adsorbed water. For proton hopping, although the fitting value (0.64 eV, δ = 0.64) is less than the computed value (0.88 eV), the range of values obtained from the two fits is quite big and the computed value is likely too large as discussed above. One might expect that in

dx.doi.org/10.1021/jp5076719 | J. Phys. Chem. A 2014, 118, 12031−12040

the limit of a heavily hydrated surface the value would approach the strength of a typical hydrogen bond (ca. 0.2 eV) as would be expected for water-assisted proton-hopping.[6,25] Finally, although the range of theoretical values for the gap in the presence of a surface O vacancy is broad, [0.07−1.92 eV] the fitting value (0.38 eV, δ = 0.28) does fall within the range of theoretically predicted values.

The above comparison of fitting values to theoretical results confirms that the surface conductance model captured by eq 11 is physically reasonable. The theoretical calculations also show that upon dissociative water adsorption, the two hydroxyl groups formed at the surface interact through hydrogen bonding. Application of the Langmuir equation (6) shows that under standard conditions, $\Theta_w \approx 1$, and therefore, the [110] surface of tin dioxide is essentially completely covered with hydrogen-bonded hydroxyl groups, confirming the supposition to this effect in the previous paragraph. These interacting hydroxyl groups can serve as a scaffold for proton hopping.[6,8] Combining these results, it may be concluded that mobile protons freed by the dissociative adsorption of water at the [110] surface are potential charge carriers in the "freeze out" temperature region and the likely source of the anomalous "bump" in the ln $G(T)$ curve ca. 400 K. Between 300 and 400 K, the dominant charge carriers are mobile surface protons. As the thermal energy increases, the probability increases that a proton will overcome the hopping barrier. This corresponds to an increase in the mobility and, consequently, the conductivity arising from the protons. Between 400 and 450 K, water molecules undergo thermal desorption, removing the scaffold that supports charge transport by protons. At temperatures higher than 450 K, protonic conduction is no longer dominant and conduction is generated by the formation of bridging oxygen vacancies, which significantly reduce the band gap and lead to population of the conduction band. Figure 8 shows how the protonic and electronic factors combine to produce the overall ln $G(T)$ curve with an anomalous "bump" ca. 400 K.

Both bulk and bridging oxygen vacancies produce occupied energy bands that fall within the band gap (see the band diagrams and associated DOS figures in the Supporting Information) but the electronic structure calculations reported here show that surface oxygen vacancies occur with a lower energy cost and are likely the dominant source of conduction band electrons. This holds true for all the levels of density functional theory applied in this study.

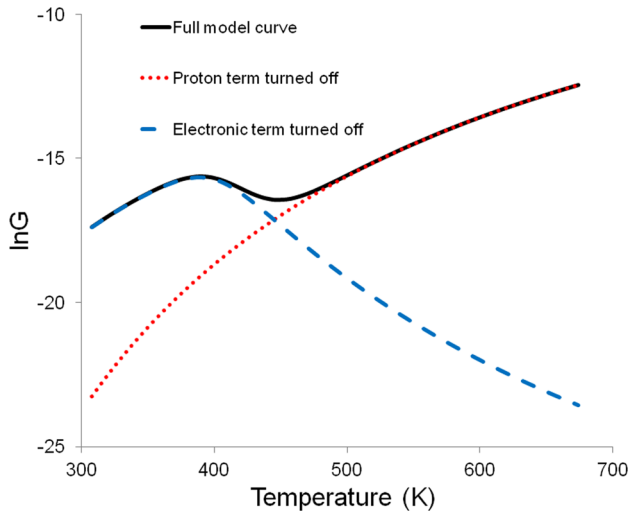

Figure 8. Full model curve, the model curve with the proton term turned off, and the model curve with the electronic term turned off for data set 1.

The band gap of SnO_2 decreases at the [110] surface as indicated by the fact that $E_{G,s}/E_G < 1.0$. According to eq 11, as a consequence of this band gap decrease at the surface, the concentration of electrons in the conduction band increases at the surface. Therefore, increasing the surface area of tin dioxide should improve its conductance, an effect that has been reported for other metal oxides.[17]

There has been some discussion in the literature about the possible role of adsorbed water in contributing to, or depleting from, electron population in the conduction band. Experimental studies by Semancik and Cox[54] reveal downward band bending following water adsorption at the [110] surface of tin dioxide. This finding suggests that electrons are transferred from water to tin dioxide. Santarossa et al.[49] performed finite temperature molecular dynamics simulations to examine the adsorption of water at the same surface of tin dioxide. Using projected density of states calculations, they found electron transfer from tin dioxide to water accompanies dissociative water adsorption. They observed the transfer in the opposite direction for nondissociative water adsorption.

Figure 9 shows computed density of states plots for clean and hydrated [110] surfaces of SnO_2 near the conduction band minimum.

This comparison clearly indicates that there is but a nominal difference between the density of states for dissociative (red) and nondissociative (green) water adsorption near the conduction band minimum. Figure 9 also shows that the densities of states for the clean and hydrated [110] surfaces are also quite similar. This finding supports the conclusion that the presence of surface water enhances conductance by generating protonic as opposed to electronic charge carriers. The present calculations do not refute that some electron transfer may occur following the adsorption of water to the [110] surface of tin dioxide, but it seems likely that protonic conduction contributes more significantly to the thermal dependence of conductance for tin dioxide because water adsorption leads to relatively minor changes in the electronic structure.

5. CONCLUSIONS

A mathematical model for the thermal dependence of conductance of SnO_2 that includes contributions from both electron transport and proton hopping accounts for the anomalous "bump" ca. 400 K that appears in the experimental ln G vs T^{-1} curve for tin dioxide. By combining the model with theoretical calculations of the interaction of water with the SnO_2 (110) surface, it may be concluded that mobile protons, freed from the dissociative adsorption of water on the surface, are an essential component of the observed thermal dependence of surface conductance in tin dioxide. Below about 400 K the mobility of these protons increases as the available thermal energy increases leading to an increase in conductance. Between 400 and 450 K, however, the surface-adsorbed water undergoes thermal desorption, removing the scaffold that supports charge transport by protons and this contribution to conductance is lost. At temperatures higher than 450 K conventional semiconductor transport governs conductance. These findings imply that variations in humidity could significantly alter the conductance of tin dioxide devices that operate between 300 and 450 K.

dx.doi.org/10.1021/jp5076719 | J. Phys. Chem. A 2014, 118, 12031−12040

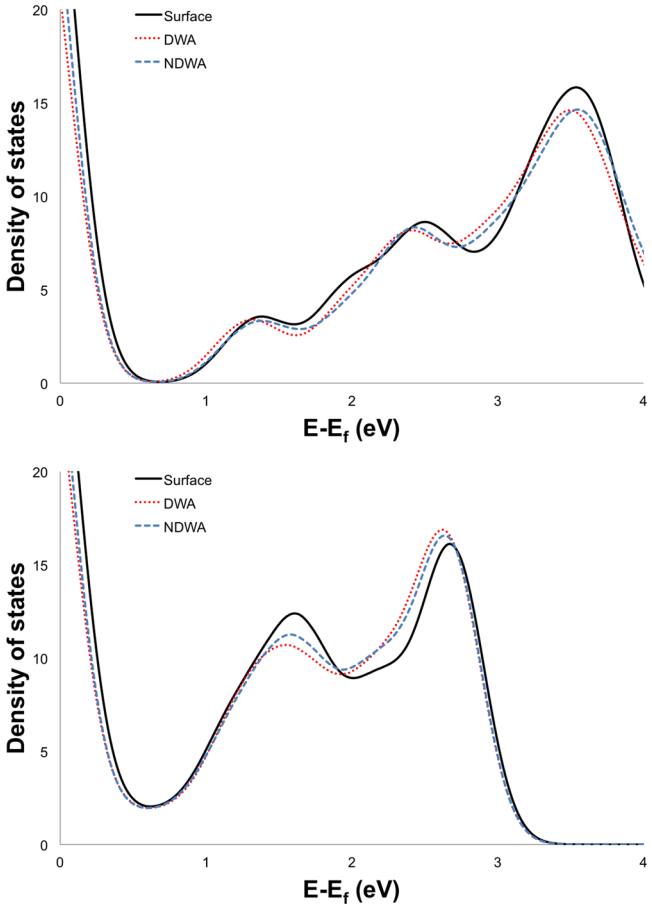

Figure 9. DFT-LDA/CA-PZ (top) and -GGA/PBE (bottom) density of states plots for the [110] surface of tin dioxide, dissociative water adsorption ("DWA"), and nondissociative water adsorption ("NDWA").

■ ASSOCIATED CONTENT

Ⓢ Supporting Information

Supporting Information includes sensitivity of the fit with respect to variations in the parameters, k-point grids used in DFT calculations, band structures, and density of states plots. Animation of the computed hopping path for a proton on the surface of tin dioxide. This material is available free of charge via the Internet at http://pubs.acs.org.

■ AUTHOR INFORMATION

Corresponding Author

*Karl Sohlberg. Office: Disque Hall 222. Phone: 215-895-2653. E-mail: sohlbergk@drexel.edu. Fax: 215-895-6951.

Present Address

†R. B. Wexler. Department of Chemistry, University of Pennsylvania, Philadelphia, PA 19104. Office: Chemistry 1941 141A. Phone: 215-573-4241.

Author Contributions

The manuscript was written through contributions of all authors. All authors have given approval to the final version of the manuscript.

Notes

The authors declare no competing financial interest.

■ ACKNOWLEDGMENTS

R.B.W. was supported in part by a fellowship from the Steinbright Career Development Center.

■ REFERENCES

(1) Kim, H.; Gilmore, C. M.; Pique, A.; Horwitz, J. S.; Mattoussi, H.; Murata, H.; Kafafi, Z. H.; Chrisey, D. B. Electrical, Optical, And Structural Properties of Indium−Tin−Oxide Thin Films for Organic Light-Emitting Devices. *J. Appl. Phys.* **1999**, *86* (11), 6451−6461.

(2) Batzill, M.; Diebold, U. The Surface and Materials Science of Tin Oxide. *Prog. Surf. Sci.* **2006**, *79*, 47−154.

(3) Harrison, P. G.; Willett, M. J. The Mechanism of Operation of Tin(IV) Oxide Carbon Monoxide Sensors. *Nature* **1988**, *332* (6162), 337−339.

(4) Stoica, M.; Caldararu, M.; Ionescu, N. I.; Auroux, A. Protonic Conductivity of Pt/Al_2O_3 in Hydrogen- And Water-Containing Atmospheres. *Appl. Surf. Sci.* **2000**, *153* (4), 218−222.

(5) Caldararu, M.; Postole, G.; Hornoiu, C.; Bratan, V.; Dragan, M.; Ionescu, N. I. Electrical Conductivity of γ-Al_2O_3 at Atmospheric Pressure under Dehydrating/Hydrating Conditions. *Appl. Surf. Sci.* **2001**, *181* (3), 255−264.

(6) Cai, S.; Caldararu, M.; Chihaia, V.; Munteanu, C.; Hornoiu, C.; Sohlberg, K. Possible Dual-Charge-Carrier Mechanism of Surface Conduction on γ-Alumina. *J. Phys. Chem. C* **2007**, *111* (14), 5506−5513.

(7) Cai, S.; Caldararu, M.; Sohlberg, K. Entropic Contributions to the Atomic-Scale Charge-Carrier/Surface Interactions That Govern Macroscopic Surface Conductance. *J. Phys. Chem. C* **2010**, *114* (9), 3991−3997.

(8) Kavasoglu, N.; Bayhan, M. Air Moisture Sensing Properties of $ZnCr_2O_4$-K_2CrO_4 Composites. *Turk. J. Phys.* **2005**, *29*, 249−255.

(9) Xing, W.; Kalland, L.-E.; Li, Z.; Haugsrud, R. Defects and Transport Properties in $TiNb_2O_7$. *J. Am. Ceram. Soc.* **2013**, *96* (12), 3775−3781.

(10) Sapurina, I. Y.; Kompan, M. E.; Zabrodskii, A. G.; Stejskal, J.; Trchova, M. Nanocomposites with Mixed Electronic and Protonic Conduction for Electrocatalysis. *Russ. J. Electrochem.* **2007**, *43* (5), 528−536.

(11) Sharma, A.; Prakash, D.; Verma, K. Optical Characterization of Hydrothermally Grown SnO_2 Nanocrystals. *J. Optoelectron. Adv. Mater.* **2009**, *11* (3), 331−337.

(12) Caldararu, M.; Chihaia, V.; Sohlberg, K.; Munteanu, C.; Hornoiu, C.; Carata, M. Water and Proton Mobility on γ-Alumina and Sn/γ-Alumina: a Combined Electrical Conductivity and Semiempirical PM3 Study. *Prog. Catal.* **2005**, *14* (1−2), 9−20.

(13) Lantto, V.; Rompplainen, P.; Leppävuori, S. A Study of the Temperature Dependence of the Barrier Energy in Porous Tin Dioxide. *Sens. Actuators* **1988**, *14* (2), 149−163.

(14) Schmitte, F. J.; Wiegleb, G. Conductivity Behaviour of Thick-Film Tin Dioxide Gas Sensors. *Sens. Actuators, B* **1991**, *4* (3−4), 473−477.

(15) Fleischer, M.; Meixner, H. Sensing Reducing Gases at High Temperatures Using Long-Term Stable Ga_2O_3 Thin Films. *Sens. Actuators, B* **1992**, *6* (1−3), 257−261.

(16) Scurtu, M.; Hornoiu, C.; Caldararu, M.; Munteanu, C.; Postole, G.; Ionescu, N. I.; Yuzhakova, T.; Redey, A. Influence of the Reactant Gas on the Electrical Properties of Alumina-Supported Tin Dioxide Catalysts. *Reaction Kinetics, Mechanisms and Catalysis* **2012**, *105* (1), 163−172.

(17) Caldararu, M.; Hornoiu, C.; Postole, G.; Dragan, M.; Carata, M.; Ionescu, N. I.; Petre, A.; Auroux, A. In *In situ electrical conductivity revisited for catalyst characterization*; Petrov, L., Bonev, C., Eds.; 2000 UNIDO Workshop on "Catalysis for Sustainable Chemistry: Structure, Processes and Industrial Applications", Sofia, Bulgaria, 2001; Star Press: Sofia: Sofia, Bulgaria, 2001; p 71.

(18) Shen, Y.; Nishida, M.; Kanematsu, W.; Hibino, T. Synthesis and Characterization of Dense SnP_2O_7-SnO_2 Composite Ceramics As

Intermediate-Temperature Proton Conductors. *J. Mater. Chem.* **2010**, *21* (3), 663−670.
(19) Pierret, R. F.; Neudeck, G. W. *Advanced Semiconductor Fundamentals*; Addison-Wesley: Reading, MA, 1987.
(20) Kim, K. H.; Park, C. G. Electrical Properties and Gas-Sensing Behavior of SnO_2 Films Prepared by Chemical Vapor Deposition. *J. Electrochem. Soc.* **1991**, *138* (8), 2408−2412.
(21) Langmuir, I. The Constitution and Fundamental Properties of Solids and Liquids. Part I. Solids. *J. Am. Chem. Soc.* **1916**, *38* (11), 2221−2295.
(22) Sohlberg, K.; Pennycook, S. J.; Pantelides, S. T. Hydrogen Mobility in Catalytic Aluminas: Theory and Implications. *Recent Res. Dev. Phys. Chem.* **2000**, *4* (part I), 71−81.
(23) Matsushita, E.; Tanase, A. Conduction Mechanism in Transition-Metal Oxides. *Physica B: Condens. Matter* **1997**, *237*−*238* (0), 21−23.
(24) Matsushita, E.; Sasaki, T. Theoretical Approach for Protonic Conduction in Perovskite-Type Oxides. *Solid State Ionics* **1999**, *125* (1−4), 31−37.
(25) Tocci, G.; Michaelides, A. Solvent-Induced Proton Hopping at a Water-Oxide Interface. *J. Phys. Chem. Lett.* **2014**, *5* (3), 474−480.
(26) Ceperley, D. M.; Alder, B. J. Ground State of the Electron Gas by a Stochastic Method. *Phys. Rev. Lett.* **1980**, *45* (7), 566−569.
(27) Perdew, J. P.; Zunger, A. Self-Interaction Correction to Density-Functional Approximations for Many-Electron Systems. *Phys. Rev. B* **1981**, *23* (10), 5048−5079.
(28) Perdew, J. P.; Burke, K.; Ernzerhof, M. Generalized Gradient Approximation Made Simple. *Phys. Rev. Lett.* **1996**, *77* (18), 3865−3868.
(29) *CASTEP, Discovery Studio Modeling Environment*, Release 3.5; Accelrys Software Inc.: San Diego, CA, 2012.
(30) Becke, A. D. Density-Functional Thermochemistry. III. The Role of Exact Exchange. *J. Chem. Phys.* **1993**, *98* (7), 5648−5652.
(31) Stephens, P. J.; Devlin, F. J.; Chabalowski, C. F.; Frisch, M. J. Ab Initio Calculation of Vibrational Absorption and Circular Dichroism Spectra Using Density Functional Force Fields. *J. Phys. Chem.* **1994**, *98* (45), 11623−11627.
(32) Dovesi, R.; Orlando, R.; Civalleri, B.; Roetti, C.; Saunders, V. R.; Zicovich-Wilson, C. M. CRYSTAL: a Computational Tool for the Ab Initio Study of the Electronic Properties of Crystals. *Z. Kristallogr.* **2005**, *220*, 571−573.
(33) Causa, M.; Dovesi, R.; Roetti, C. Pseudopotential Hartree-Fock study of Seventeen III-V and IV-IV Semiconductors. *Phys. Rev. B* **1991**, *43* (14), 11937−11943.
(34) Durand, P.; Barthelat, J.-C. A Theoretical Method to Determine Atomic Pseudopotentials for Electronic Structure Calculations of Molecules and Solids. *Theor. Chim. Acta* **1975**, *38* (4), 283−302.
(35) Causa, M.; Dovesi, R.; Pisani, C.; Roetti, C. Electronic Structure and Stability of Different Crystal Phases of Magnesium Oxide. *Phys. Rev. B* **1986**, *33* (2), 1308−1316.
(36) Stewart, J. J. P. Optimization of Parameters for Semiempirical Methods V: Modification of NDDO Approximations and Application to 70 Elements. *J. Mol. Modeling* **2007**, *13*, 1173−1213.
(37) Trani, F.; Causa, M.; Ninno, D.; Cantele, G.; Barone, V. Density Functional Study of Oxygen Vacancies at the SnO_2 Surface and Subsurface Sites. *Phys. Rev. B* **2008**, *77* (24), 245410.
(38) Batzill, M.; Katsiev, K.; Burst, J. M.; Diebold, U.; Chaka, A. M.; Delley, B. Gas-Phase-Dependent Properties of SnO_2 (110), (100), and (101) Single-Crystal Surfaces: Structure, Composition, and Electronic Properties. *Phys. Rev. B* **2005**, *72* (16), 165414.
(39) Han, X.; Jin, M.; Xie, S.; Kuang, Q.; Jiang, Z.; Jiang, Y.; Xie, Z.; Zheng, L. Synthesis of Tin Dioxide Octahedral Nanoparticles with Exposed High-Energy {221} Facets and Enhanced Gas-Sensing Properties. *Angew. Chem., Int. Ed.* **2009**, *48* (48), 9180−9183.
(40) Stroppa, D. G.; Montoro, L. A.; Beltran, A.; Conti, T. G.; da Silva, R. O.; Andres, J.; Leite, E. R.; Ramirez, A. J. Anomalous Oriented Attachment Growth Behavior on SnO_2 Nanocrystals. *Chem. Commun.* **2011**, *47* (11), 3117−3119.
(41) Tanaka, I.; Oba, F.; Tatsumi, K.; Kunisu, M.; Nakano, M.; Adachi, H. Theoretical Formation Energy of Oxygen-Vacancies in Oxides. *Mater. Trans.* **2002**, *43* (7), 1426−1429.
(42) Oviedo, J.; Gillan, M. J. The Energetics and Structure of Oxygen Vacancies on the SnO_2(110) Surface. *Surf. Sci.* **2000**, *467*, 35−48.
(43) Vlček, L.; Cummings, P. T. Adsorption of Water on TiO_2 and SnO_2 Surfaces: Molecular Dynamics Study. *Collect. Czech. Chem. Commun.* **2008**, *73*, 575−589.
(44) Hahn, K. R.; Tricoli, A.; Santarossa, G.; Vargas, A.; Baiker, A. First Principles Analysis of H_2O Adsorption on the (110) Surfaces of SnO_2, TiO_2 and Their Solid Solutions. *Langmuir* **2012**, *28* (2), 1646−1656.
(45) Sensato, F. R.; Custodio, R.; Calatayud, M.; Beltran, A.; Andres, J.; Sambrano, J. R.; Longo, E. Periodic Study on the Structural and Electronic Properties of Bulk, Oxidized and Reduced SnO_2(110) Surfaces and the Interaction With O_2. *Surf. Sci.* **2002**, *511* (1−3), 408−420.
(46) Singh-Miller, N. E.; Marzari, N. Surface Energies, Work Functions, And Surface Relaxations of Low-Index Metallic Surfaces from First Principles. *Phys. Rev. B* **2009**, *80* (23), 235407.
(47) Michealides, A.; Scheffler, M., An Introduction to the Theory of Crystalline Elemental Solids and their Surfaces. In *Surface and Interface Science: Concepts and Methods*; Wandelt, K., Ed.; Wiley-VCH: Weinheim, 2012; pp 13−72.
(48) Taylor, P. L.; Heinonen, O. *A Quantum Approach to Condensed Matter Physics*; Cambridge University Press: Cambridge, U.K., 2002.
(49) Santarossa, G.; Hahn, K.; Baiker, A. Free Energy and Electronic Properties of Water Adsorption on the SnO_2(110) Surface. *Langmuir* **2013**, *29* (18), 5487−5499.
(50) Peng, C.; Schlegel, H. B. Combining Synchronous Transit and Quasi-Newton Methods for Finding Transition States. *Isr. J. Chem.* **1993**, *33*, 449−454.
(51) Janesko, B. G.; Scuseria, G. E. Hartree-Fock Orbitals Significantly Improve the Reaction Barrier Heights Predicted by Semilocal Density Functionals. *J. Chem. Phys.* **2008**, *128* (24), 244112.
(52) Andersson, S.; Grüning, M. Performance of Density Functionals for Calculating Barrier Heights of Chemical Reactions Relevant to Astrophysics. *J. Phys. Chem. A* **2004**, *108* (37), 7621−7636.
(53) Schroeder, S.; Thiel, W. Comparison of Semiempirical and Ab Initio Transition States. *J. Am. Chem. Soc.* **1985**, *107* (15), 4422−4430.
(54) Semancik, S.; Cox, D. F. Fundamental Characterization of Clean and Gas-Dosed Tin Oxide. *Sens. Actuators* **1987**, *12* (2), 101−106.